A Dual Grating Fiber Sensor to Discriminate Axial and Radial Strains

Romain Guyard, Dominique Leduc, Yann Lecieux and Cyril Lupi

Institut de Génie Civil et de Mécanique (GeM), l'UNAM Université,
Université de Nantes, UMR CNRS 6183,
Email: Romain.Guyard@univ-nantes.fr

***Abstract*—When a fiber Bragg grating strain sensor is embedded inside a structure, the interaction of the sensor with the host material can lead to spurious results if the radial strain is neglected. In this article, we use numerical simulations to show that the axial and radial strains can be simultaneously measured with a single fiber in which a Bragg grating and a long period grating are superimposed. Moreover, we present an optimal architecture of the sensor.**

Keywords–Strain; Embedded sensors; optical fiber gratings.

I. INTRODUCTION

Fiber Bragg gratings (FBG) are made of periodic modulation of the refractive index of the core of an optical fiber. As a consequence they behave as bandpass filters and reflect a very narrow spectral band of the incoming light, centered on the Bragg wavelength : $\lambda_B = 2n_{\text{eff}}\Lambda_0$ where n_{eff} is the effective index of the light propagating inside the core and Λ_0 the period of the grating. Any change in the period of the grating or in the effective index induces a shift in the Bragg wavelength.

FBGs are often used as strain sensors (see for example [1]–[5]). Indeed, when the fiber is strained, the period of the grating is modified. Moreover, due to the photo-elastic effect, the effective index also varies. What should be underlined is that the variation of the effective index depends on the strains in all directions. There is a tensorial relation between strain and refractive index change.

When the fiber is glued at two points on the surface of the monitored structure, its *axial* strain, ϵ_z, is exactly the same as the strain of the structure. Moreover, as the fiber is free to deform in the transverse plane, its *radial* strain ϵ_r is driven by the axial strain: $\epsilon_r = -\nu\epsilon_z$, where ν is the Poisson's ratio of the fiber. In this case, the axial strain is the only unknown and the measurement of a single Bragg wavelength shift is then sufficient. This is why FBG strain sensors are usually mounted at the surface of the structure.

When the fiber is embedded, it is not free anymore to deform in the transverse plane. Its radial strain then depends in a non trivial manner on the interaction between the fiber and the host material. It can not be deduced simply from the axial strain. Consider for example a sensor embedded in a cylinder of heat hardening resin (Young modulus: 3100 MPa, Poisson's ration: 0.4; thermal expansion coefficient: 114×10^{-6} K^{-1}) as used in the composite material. The initially liquid resin is heated. During cooling, it imposes mechanical stress on the fiber axially as well as radially. Assume that a drop of 100 K in temperature is imposed on the structure, with two different boundary conditions (BC): BC 1: the cylinder is free to undergo axial and radial deformation; BC 2: the cylinder external surface is free to move radially while the upper and lower sections are fixed. Table I shows the calculated axial and radial strains together with the radial strain that would be measured by a single FBG under the assumption that: $\epsilon_r = -\nu\epsilon_z$. These results show that a single embedded FBG

TABLE I. Comparisons between calculated and measured strains

	BC 1		BC 2	
	axial strain	radial strain	axial strain	radial strain
Calcul	-11400 $\mu\epsilon$	1562 $\mu\epsilon$	0 $\mu\epsilon$	-438 $\mu\epsilon$
FBG	-11200 $\mu\epsilon$		209 $\mu\epsilon$	

gives at best approximate measurements (BC 1) and sometimes erroneous measurements (BC 2). A real case is in between BC 1 and BC 2. This underlines that the axial and the radial strains must be simulteaneously determined. Then two linearly independant measurements have to be performed at the same point. It has been recently proposed to use the superposition of a long and a short period grating to achieve this task [6]. In this paper we study numerically more deeply this architecture and show that some configurations can fullfill the following requirements:

- The sensor has to measure simultaneously the radial and axial strains with the same precision on the axial strain as the FBGs mounted on surface.
- The transmission spectrum of the sensor has to exhibit only two peaks in the range [1400 nm; 1600 nm], one associated to the FBG and one to the Long Period Grating (LPG) in order to avoid any ambiguity in the order of the mode of the LPG.
- The response of the sensor must be linear in the range $\epsilon_{r,z} \in [-\,5000\ \mu\epsilon; +\,5000\ \mu\epsilon]$.

Section 2 is devoted to the description of the sensor and of the principle of measurement. In Section 3, we present the evolution of the behavior of the sensor as a function of relevant parameters and we determine the best architectures. Then we conclude and discuss briefly the results in Section 4.

II. THE DUAL GRATING SENSOR

In this section, we present the structure of sensor and we describe the principle of measurement.

A. Architecture of the sensor

The sensor is made of the juxtaposition of two gratings of same length inside the core of a fiber, surrounded by two concentric claddings (see Figure 1). Both gratings can be written using UV light with the same phase mask technique. The best is to write first the Bragg grating with one mask and then the long period grating with another mask [7].

We call a_1 the radius of the core and n_1 its refractive index, a_2 the radius of the inner cladding and n_2 its index, and a_3 the

 ISBN: 978-1-61208-426-8

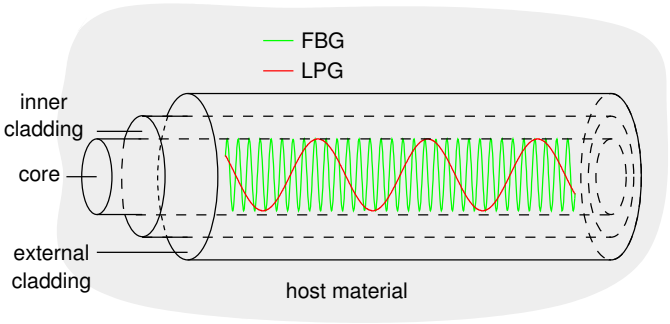

Figure 1. (a) Geometry of sensor. The red and green lines represent the variation of the refractive index of the core corresponding to the LPG and the FBG.

radius of the external cladding and n_3 its index. In order that only one mode propagates in the core of the fiber, the values of a_1, n_1 and n_2 are fixed to that of a classical SMF28 fiber:

$$a_1 = 4.2\,\mu m \quad \text{and} \quad n_1 = 1.0036 n_2 \tag{1}$$

where n_2 is given by the Sellmeier's law:

$$n_2^2(\lambda) = 1 + \sum_{i=0}^{3} \frac{A_i \lambda^2}{\lambda^2 - \lambda_i^2} \tag{2}$$

with $A_1 = 0.696750$, $A_2 = 0.408218$, $A_3 = 0.890815$, $\lambda_1 = 0.069066\,\mu m$, $\lambda_2 = 0.115662\,\mu m$ and $\lambda_3 = 9.900559\,\mu m$ [8].

The first grating is a classical fiber Bragg grating. It reflects a narrow bandwidth of the incoming light centered on the Bragg wavelength λ_B. As a consequence, its transmission spectrum exhibit a hole around λ_B. The value of λ_B is given by the condition of resonance:

$$\lambda_B = 2 n_{\text{eff}}^{\text{core}}(a_1,\, n_1,\, n_2, \lambda_B)\, \Lambda_B \tag{3}$$

where Λ_B is the period of the grating and $n_{\text{eff}}^{\text{core}}$ the effective index of the mode that propagates inside the core. It is given by the dispersion equation [9]:

$$F_c(a_1, n_1, n_2, n_{\text{eff}}^{\text{core}}, \lambda) = 0 \tag{4}$$

The second grating is a long period grating which couples the mode inside the core to resonnant inner cladding modes. The wavelengths of resonant cladding modes are given by:

$$\lambda_{LPG} = \left[n_{\text{eff}}^{\text{core}}(a_i,\, n_i, \lambda_{LPG}^m) - n_{\text{eff,m}}^{\text{clad}}(a_i,\, n_i, \lambda_{LPG}^m)\right] \Lambda_{\text{LPG}} \tag{5}$$

where Λ_{LPG} is the period of the grating and $n_{\text{eff,m}}^{\text{clad}}$ the effective index of the m^{th} cladding mode. It is given by the dispersion equation of the cladding modes [9]:

$$F_g\left(a_1, a_2, n_1, n_2, n_3, n_{\text{eff}}^{\text{core}}, n_{\text{eff}}^{\text{clad}}, \lambda\right) = 0 \tag{6}$$

The light propagating inside the cladding gradually vanishes because of inhomogeneities and micro-bending. The transmission spectrum of the LPG exhibits then holes around each λ_{LPG}.

The coupling coefficient κ^m between a cladding mode m and the core mode [10]:

$$\kappa^m = \frac{\omega \epsilon_0 n_1^2}{2} \int_0^{2\pi} d\theta \int_0^{a_1} r dr\, E_t^m . E_{0t}^* \tag{7}$$

gives the strenght of the coupling and then the depth of the hole in the spectrum.

B. Principle of measurement

When the fiber is strained, the period of the gratings, the radii and the indices of the three layers change. The variation of the period of each grating depends on the axial strain:

$$\Lambda = (1 + \epsilon_z)\, \Lambda_0 \tag{8}$$

where Λ_0 is the period of the grating at rest, while the changes of the radii depend on the radial strain:

$$a_i = (1 + \epsilon_r)\, a_{0i} \quad i = \{1, 2, 3\} \tag{9}$$

where a_{0i} is the radius at rest of the layer i. The variation of the refractive indices depends on both strains, due to the photo-elastic effect:

$$n_i = n_{i0} - \frac{n_{i0}^3}{2}\left[(p_{11} + p_{12})\,\epsilon_r + p_{11}\epsilon_z\right] \qquad i = \{1, 2, 3\} \tag{10}$$

where $p_{11} = 0.113$, $p_{12} = 0.252$ are the components of the photoelastic tensor of silica [11]. According to (4) and (6), the variations of the radii and the refractive indices induce a variation of the effective indices of the core mode and the cladding modes. All these changes cause a shift in λ_B and λ_{LPG} which can be expressed in the linear regime as:

$$\begin{cases} \Delta\lambda_B &= \alpha_{1r}\epsilon_r + \alpha_{1z}\epsilon_z \\ \Delta\lambda_{LPG} &= \alpha_{2r}\epsilon_r + \alpha_{2z}\epsilon_z \end{cases} \tag{11}$$

where α_{1r} and α_{1z} are respectively the sensitivity of the FBG to the radial and axial strain, and α_{2r} and α_{2z} are respectively the sensitivity of the LPG to the radial and axial strain. In a real experiment, one would measure these two shifts in wavelength and deduce the strains by inverting the system given by (11):

$$\begin{cases} \epsilon_z &= \dfrac{\alpha_{1r}\Delta\lambda_{LPG} - \alpha_{2r}\Delta\lambda_B}{D} \\ \epsilon_r &= \dfrac{\alpha_{1z}\Delta\lambda_B - \alpha_{2z}\Delta\lambda_{LPG}}{D} \end{cases} \tag{12}$$

where $D = \alpha_{1r}\alpha_{2z} - \alpha_{2r}\alpha_{1z}$.

The smallest measurable axial $\Delta\epsilon_z$ and radial $\Delta\epsilon_r$ strains can be derived from (12) using an uncertainty calculation:

$$\begin{cases} \Delta\epsilon_z &= \dfrac{|\alpha_{1r}| + |\alpha_{2r}|}{|D|}\delta\lambda_{min} \\ \Delta\epsilon_r &= \dfrac{|\alpha_{1z}| + |\alpha_{2z}|}{|D|}\delta\lambda_{min} \end{cases} \tag{13}$$

where $\delta\lambda_{min}$ is the smallest measurable wavalength shift. It is usually of the order of 1 pm. Equation 13 shows that the largest D is, the better the resolution is.

C. Method to determine optimal architecture

The aim of the study is to find an architecture that meets the specifications. The parameters are a_1, a_2, a_3, n_1, n_2, n_3, λ_B and λ_{LPG}. The number of parameters can be reduced with the help of physical considerations. As stated above, the characteristics of the core and the refractive index of the inner cladding are choosen to be the same of a single mode SMF28 fiber. The outer cladding serves to isolate the modes of the inner cladding from the environment of the fiber. Its radius must be sufficiently large so that the cladding modes amplitudes falls to zero well before the interface between the outer cladding and the external medium. In practice, $a_3 = a_2 + 15\ \mu m$ is enough. In contrast, the refractive index of the outer cladding n_3 influences very little the properties of

 ISBN: 978-1-61208-426-8

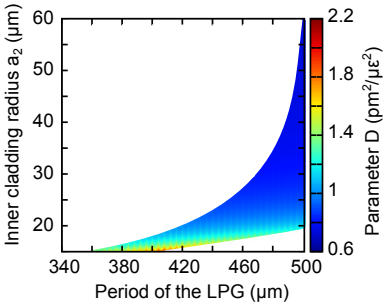

(a) Mode 1 : D

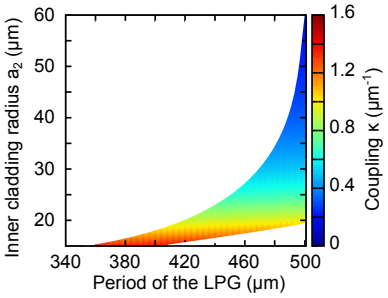

(b) Mode 1 : κ

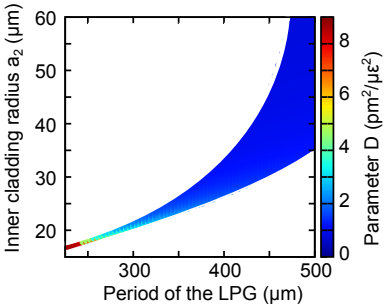

(c) Mode 3 : D

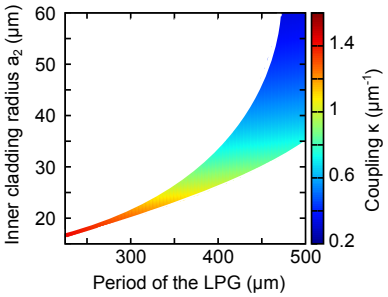

(d) Mode 3 : κ

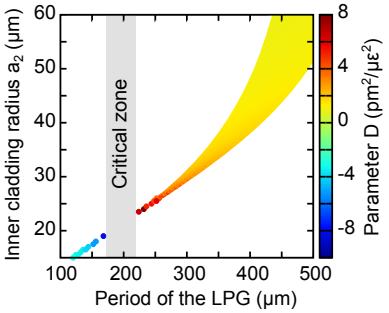

(e) Mode 5 : D

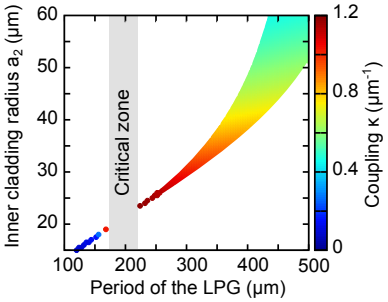

(f) Mode 5 : κ

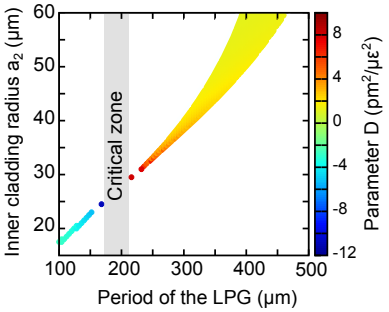

(g) Mode 7 : D

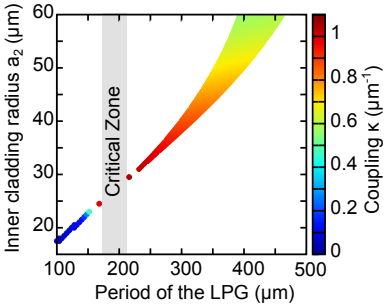

(h) Mode 7 : κ

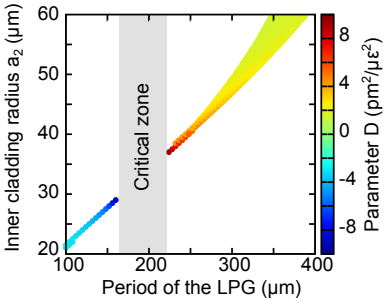

(i) Mode 9 : D

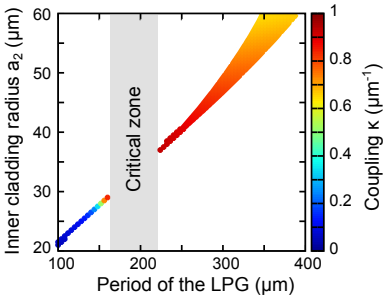

(j) Mode 9 : κ

Figure 2. Evolution of D and κ as a function of a_2 and Λ_{LPG}.

 ISBN: 978-1-61208-426-8

the grating. It can be choosen arbitrarily in the range $[1.; n_2[$. We use the value $n_3 = 0.95n_2$ compatible with silica. The period of the Bragg grating is fixed to 501 nm in order to obtain a Bragg wavelength of 1.45 μm. Finally, the only free parameters are a_2 and Λ_{LPG}.

In order to determine the best couples of parameters $\{a_2, \Lambda_{LPG}\}$, we proceeded to a systematic exploration of the parameters space, with Λ_{LPG} varying from 100 μm to 500 μm by steps of 5 μm and a_2 varying from 15 μm to 70 μm by steps of 0.5 μm. Values of a_2 smaller than 15 μm were not considered because in this case the inner cladding is not large enough to isolate the core mode from the outer cladding.

For each couple $\{a_2, \Lambda_{LPG}\}$, we first determined the wavelength of the resonant cladding modes of the unstrained sensor using (5) and (6). We only kept the couples for which only one mode was present in the range [1400 nm, 1600 nm]. Then we applied a radial strain comprised in the range $[-5000\ \mu\epsilon; +5000\ \mu\epsilon]$, the axial strain remaining null. For each strain, the new radii and indices were calculated with the help of (9), (10), (4) and (6). This led to the new λ_B and λ_{LPG} from which were deduced the shifts $\Delta\lambda_B$ and $\Delta\lambda_{LPG}$. Then a linear regression gave the sensitivity α_{1r} of the Bragg wavelength and α_{2r} of the long period grating to the radial strain. The same procedure was used to calculate the sensitivity of the FBG and the LPG to the axial strain.

III. RESULTS

Figure 2 shows a cartography of the coupling coefficient κ and the parameter D for the first five odd cladding modes, as a function of a_2 and Λ_{LPG}. Even modes are not considered since their coupling coefficient is almost zero.

The white areas in each graph correspond to configurations where λ_{LPG} is outside the range [1400 nm; 1600 nm]. For each mode and for both D and κ, the shape of the coloured area looks like a comma, which tip is close to the lowest Λ_{LPG} and the lowest a_2. Above mode 5, the tip is splitted into two parts, with a dead zone where no mode falls in the desired range. The sign of D changes throught the critical zone and the coupling coefficient abruptly falls to zero. This corresponds to a change of modal properties of the cladding.

As stated by (13), the highest sensitivity is obtained with the largest values of D. For each mode, the largest values of D are located in the tip of the comma, *i.e.*, for the smallest values of Λ_{LPG} and the smallest values of a_2. What is very interesting is that the highest coupling coefficients are also localised in the tip of the comma. This means that a couple $\{a_2, \Lambda_{LPG}\}$ can provide at the same time a good resolution and a good coupling.

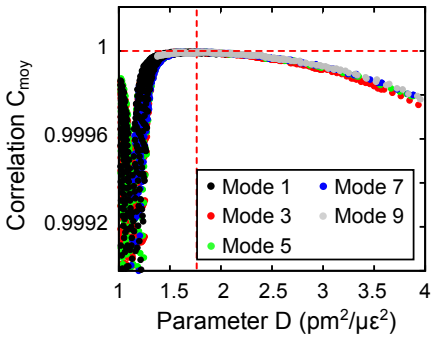

Figure 3. Evolution of C_{moy} as a function of D.

However, it is not possible to choose the configuration with the highest D since others specifications have to be fullfilled. In particular, the shifts of wavelength must evolve linearly with the strain in the range $[-5000\mu\epsilon; +5000\mu\epsilon]$. In order to quantify the linearity of the behavior of the long period grating, we use the estimate $C_{moy} = (|C_{\epsilon_r}| + |C_{\epsilon_z}|)/2$ where C_{ϵ_r} and C_{ϵ_z} are defined as:

$$C_\epsilon = \frac{\sum_{i=0}^{N} (\epsilon_i - \overline{\epsilon_i}) \left(\Delta\lambda^m_{LPG} - \overline{\Delta\lambda^m_{LPG}}\right)}{\sqrt{\sum_{i=0}^{N} (\epsilon_i - \overline{\epsilon_i})^2 \left(\Delta\lambda^m_{LPG}(\epsilon_i) - \overline{\Delta\lambda^m_{LPG}}\right)^2}} \quad (14)$$

where N is the number of samples of strain ϵ_i for which $\Delta\lambda^m_{LPG}$ was calculated and $\overline{x}$ is the mean value of x.

The Figure 3 shows the estimate C_{moy} as a function of D for modes 1 to 9. Surprisingly the values are placed on the same curve for all the modes. This curve presents a maximum for $D = 1.75\ pm^2/\mu\epsilon^2$. We choose this value for the sensor. This is not a sufficient condition to fix the couple $\{a_2, \Lambda_{\mathrm{LPG}}\}$, so we require a complimentary condition: $\lambda_{LPG} = 1.55$ μm. This value is far enough from λ_{FBG}, so that no collapsing can occur between the FBG and the LPG resonant wavelengths when the strain increases.

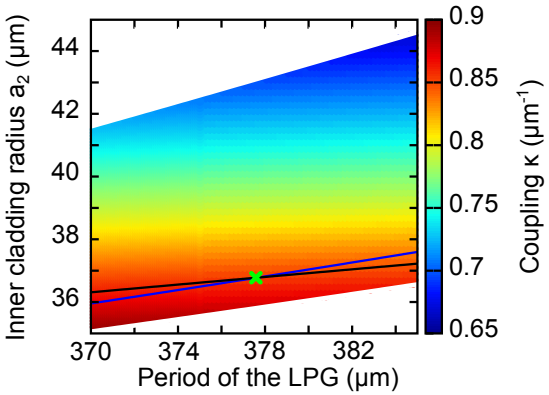

(a) m=5

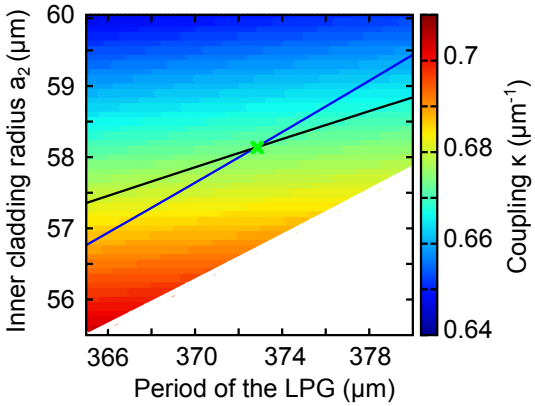

(b) m=9

Figure 4. Determination of the optimal configuration for different modes.

The dark lines on the graphics of Figure 4 correspond to the points where $D = 1.75\ pm^2/\mu\epsilon^2$ and the blue lines the points where $\lambda_{LPG} = 1.55$ μm. The intersections between these lines give the couples $\{a_2, \Lambda_{\mathrm{LPG}}\}$ that meet all the requirements. The table II summarises the characteristics of

 ISBN: 978-1-61208-426-8

long period gratings given by these intersections for the five first modes. All these gratings present very similar sensitivities α_{2r} and α_{2z} and close periods Λ_{LPG}. In contrast, they exhibit quite different coupling coefficients. The coupling coefficients of mode 1 is almost twice the coupling coefficient of mode 9. Moreover, the radius of the inner cladding for mode 1 is smaller than that of other modes which makes it less sensitive to bending. And that is an other interesting feature.

TABLE II. Characteristics of the optimal long period gratings

m	1	3	5	7	9
a_{20} (μm)	15.45	26.14	36.78	47.45	58.13
Λ_{LPG} (μm)	399.25	383.93	377.65	374.55	372.77
n_{eff}^{m}	1.442996	1.442772	1.442707	1.442672	1.442653
κ^{m} $\mu\mathrm{m}^{-1}$	1.328	1.020	0.850	0.750	0.680
α_{2r} $(pm/\mu\epsilon)$	-1.895	-1.860	-1.852	-1.847	-1.750
α_{2z} $(pm/\mu\epsilon)$	0.434	0.420	0.410	0.407	0.410

At this step, we retain two configurations: LPG1 : $\{a_{20} = 15.45\ \mu\mathrm{m},\ \Lambda_{\mathrm{LPG}} = 399.25\ \mu\mathrm{m}\}$ with mode $m = 1$ and LPG2:$\{a_{20} = 26.14\ \mu\mathrm{m},\ \Lambda_{\mathrm{LPG}} = 383.93\ \mu\mathrm{m}\}$ with mode $m = 3$. The last requirement that they have to fullfill is to present a single peak in the range [1400 nm; 1600 nm] whatever the strain.

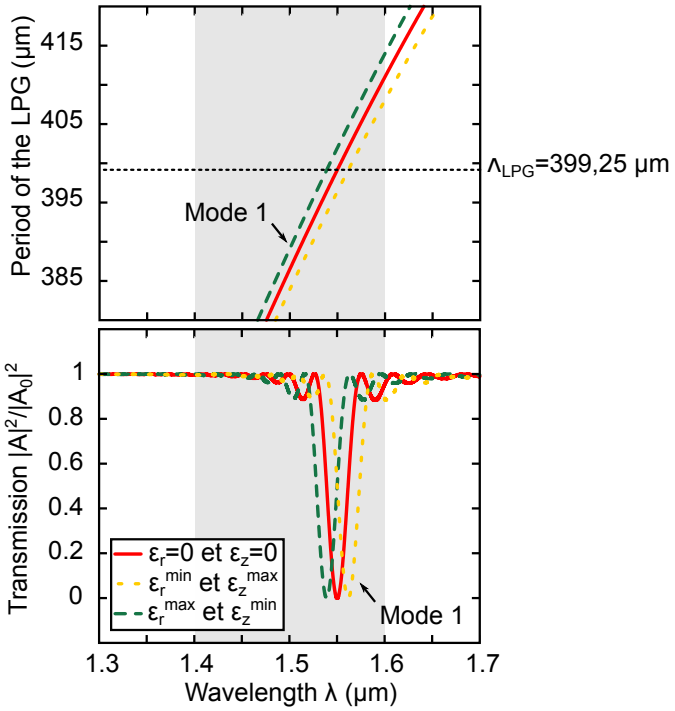

Figure 5. Evolution of λ_{LPG} with Λ_{LPG} and transmission spectrum for LPG1.

The figures 5 and 6 show the transmission spectrum of LPG1 and LPG2 together with the variation of the resonant wavelength as a function of the period of the grating: the straight line correspond to variation when the grating is at rest and the dashed lines to the maximum red-shift and the maximum blue-shift. The lengths of the gratings have been choosen to maximize the depth of the hole in the transmission spectrum. For LPG1, the mode 1 is the only one resonant in the desired wavelentgh range. In fact, no other mode is resonant in the [1300 nm, 1700 nm] for the considered range of strain. For LPG2, we can see that the modes 2 and 4 are close to

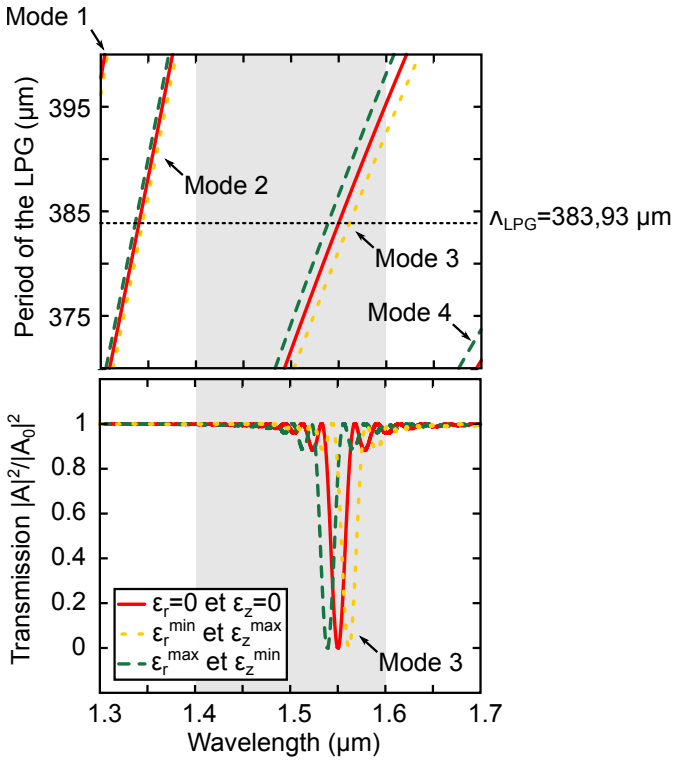

Figure 6. Evolution of λ_{LPG} with Λ_{LPG} and transmission spectrum for LPG2.

the border. However, these modes do not interfere since their coupling coefficients are negligible. These two configurations can then be used.

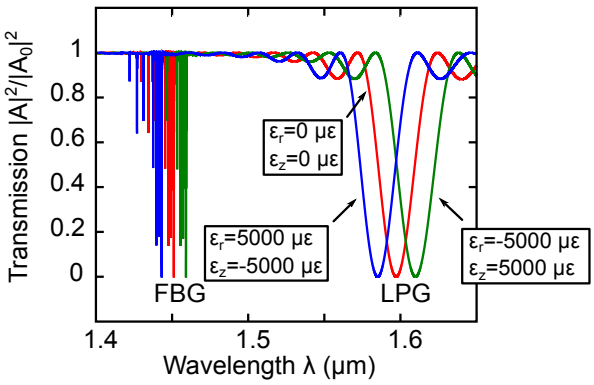

Figure 7. Transmission spectrum of optimal sensor.

We finally present on Figure 7 the whole spectrum of the sensor with LPG1. The red line correspond to the sensor at rest, the blue line to the strain that gives a maximal blue-shift and the red line to the strain that gives a maximal red-shift. We can notice a slight shift of λ_{LPG} in the absence of strain. This shift is due to the juxtaposition of the FBG. We can also notice the apparition of several narrow holes for wavelength smaller than λ_B. These holes correspond to the coupling between cladding modes and the core mode induced by the FBG. However these complementary holes do not induce confusion since their wavelengths are always smaller than λ_B.

Figure 8 shows the variation of the wavelength shifts of the FBG and the LPG as a fuction of ε_z and ε_z. As expected, the response of the sensor is quite linear. The deviation from

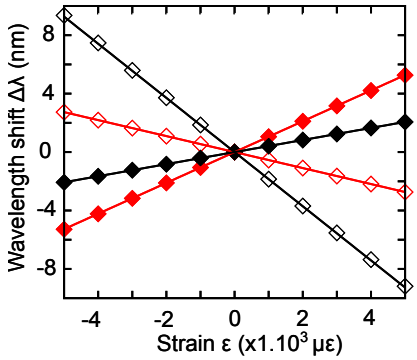

Figure 8. Response of the sensor to axial and radial strain.

linearity is drawn on Figure 9. It does not exceed 50 $\mu\epsilon$ for a strain of 5000 $\mu\epsilon$, i.e., 1%. The sensitivity of the FBG to the the axial strain is $\alpha_{1z} = 1,068\, pm/\mu\epsilon$, and that of the LPG is $\alpha_{2z} = 0,434\, pm/\mu\epsilon$. The sensitivity of the FBG to the the radial strain is $\alpha_{1r} = -0,555\, pm/\mu\epsilon$ and that of the LPG is $\alpha_{2r} = -1,895 pm/\mu\epsilon$. From this values, and assuming that the smallest measurable wavelength shift is 1 pm, we deduce from (13) that the smallest measurable radial strain is $\Delta\epsilon_r = 1,4\,\mu\epsilon$ and the smallest measurable axial strain is $\Delta\epsilon_z = 0,85\,\mu\epsilon$.

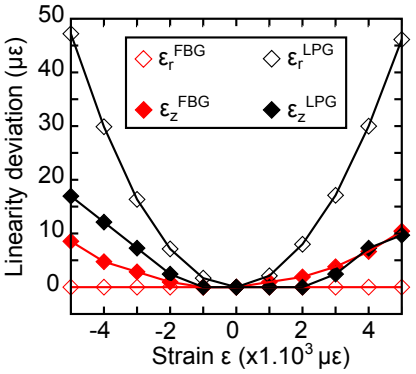

Figure 9. Deviation from linearity.

IV. Conclusion

In this article, we studied an optical fiber sensor designed to discriminate axial and radial strains when embedded in a material host. The sensor is made of the juxtaposition of a fiber Bragg grating and a long period grating inside the core of a three layer optical fiber. The specifications were to obtain a linear response of the sensor and a resolution similar to classical strain Gauge for the axial strain resolution, i.e., 1 micro-strain. Among all the parameters we identified two relevant parameters : the radius of the inner cladding and the period of the long period grating. We then searched optimal values of these parameters and found several configurations. The most promising are associated to cladding mode orders 1 and 3. These configurations present smaller radii of inner cladding which makes the sensor less sensitive to bending, and higher coupling coefficients which allows smaller lengths for the gratings. They allow to measure the axial strain with a resolution of $0,85\,\mu\epsilon$ and the radial strain with a resolution of $1,4\mu\epsilon$. This result is a real advance in strain measurement since a classical embedded strain fiber sensor can not discriminate axial and radial strain. Moreover, the resolution on axial strain of a FBG mounted on surface is of the order of $1\,\mu\epsilon$. The range of measurable strain with a linear response is [-5000 $\mu\epsilon$;+5000 $\mu\epsilon$]. In this range, the deviation from linearity is less than 1%. All these properties can make this sensor a very usefull tool for the measurement of strain inside structures. The next step is to investigate its sensitivity to bending.

References

[1] T. Chan, L. Yu, H. Tam, Y. Ni, S. Liu, W. Chung, and L. Cheng, "Fiber bragg grating sensors for structural health monitoring of tsing ma bridge: Background and experimental observation," Engineering Structures, vol. 28, no. 5, 2006, pp. 648 – 659. [Online]. Available: http://www.sciencedirect.com/science/article/pii/S0141029605003421

[2] R. Ramly, W. Kuntjoro, and M. K. A. Rahman, "Using embedded fiber bragg grating (fbg) sensors in smart aircraft structure materials," Procedia Engineering, vol. 41, no. 0, 2012, pp. 600 – 606, international Symposium on Robotics and Intelligent Sensors 2012 (IRIS 2012). [Online]. Available: http://www.sciencedirect.com/science/article/pii/S1877705812026185

[3] F. Surre, R. H. Scott, P. Banerji, P. Basheer, T. Sun, and K. T. Grattan, "Study of reliability of fibre bragg grating fibre optic strain sensors for field-test applications," Sensors and Actuators A: Physical, vol. 185, no. 0, 2012, pp. 8 – 16. [Online]. Available: http://www.sciencedirect.com/science/article/pii/S0924424712004153

[4] Y. Gebremichael, W. Li, W. Boyle, B. Meggitt, K. Grattan, B. McKinley, G. Fernando, G. Kister, D. Winter, L. Canning, and S. Luke, "Integration and assessment of fibre bragg grating sensors in an all-fibre reinforced polymer composite road bridge," Sensors and Actuators A: Physical, vol. 118, no. 1, 2005, pp. 78 – 85. [Online]. Available: http://www.sciencedirect.com/science/article/pii/S0924424704005461

[5] M. Bocciolone, G. Bucca, A. Collina, and L. Comolli, "Pantograph-catenary monitoring by means of fibre bragg grating sensors: Results from tests in an underground line," Mechanical Systems and Signal Processing, vol. 41, no. 12, 2013, pp. 226 – 238. [Online]. Available: http://www.sciencedirect.com/science/article/pii/S0888327013003142

[6] D. Leduc, Y. Lecieux, P.-A. Morvan, and C. Lupi, "Architecture of optical fiber sensor for the simultaneous measurement of axial and radial strains," Smart Materials and Structures, vol. 22, no. 7, 2013, p. 075002. [Online]. Available: http://stacks.iop.org/0964-1726/22/i=7/a=075002

[7] S. Triollet, L. Robert, E. Marin, and Y. Ouerdane, "Discriminated measures of strain and temperature in metallic specimen with embedded superimposed long and short fibre bragg gratings," Measurement Science and Technology, vol. 22, no. 1, 2011, p. 015202.

[8] V. Bhatia, "Proprieties and sensing applications of long period gratings," Ph.D. dissertation, Faculty of the Virginia Polytechnic Institute, November, 1996.

[9] T. Erdogan, "Cladding-mode resonances in short- and long-period fiber grating filters," Journal of the Optical Society of America A, vol. 14, Aug. 1997, pp. 1760–1773.

[10] H. Kogelnik, "2. theory of dielectric waveguides," in Integrated Optics. Springer, 1975, pp. 13–81.

[11] P. FERDINAND, "Capteurs fibres optiques rseaux de bragg," Techniques de l'ingnieur CND : mthodes surfaciques, vol. base documentaire : TIB586DUO., no. ref. article : r6735, 2015.

 ISBN: 978-1-61208-426-8